Design, structure, microstructure and gamma radiation shielding properties of refractory concrete materials containing Ba- and Sr-doped cements

Dominika Madej [a,*], Michał Silarski [b], Szymon Parzych [b]

[a] AGH University of Science and Technology, Faculty of Materials Science and Ceramics, Department of Ceramics and Refractories, al. A. Mickiewicza 30, 30-059, Krakow, Poland
[b] Jagiellonian University, Faculty of Physics, Astronomy and Applied Computer Science, ul. Prof. Stanisława Łojasiewicza 11, 30-348, Krakow, Poland

HIGHLIGHTS

- Ba- and Sr-doped cements belonging to the $CaO-Al_2O_3-ZrO_2$ system were proposed for heavy concretes.
- Mechanical, physical and gamma-ray attenuation properties of $(CaO,SrO,BaO)-Al_2O_3-SiO_2-ZrO_2$ concretes are presented.
- Difference in gamma ray attenuation properties of green and sintered castables was highlighted.
- Radioactive sources 22Na, 137Cs, 60Co, 133Ba and 152Eu were used in this study.
- Sr and Ba elements were chemically bonded within both hydrated cement matrix and the ceramic matrix of concrete.

ARTICLE INFO

ABSTRACT

This paper presents an experimental study on the performance of shielding refractory concretes containing new types of cements for use in the radiation protection technology. Three concretes with corundum aggregate and special refractory inorganic cements belonging to the $CaO–Al_2O_3$, $SrO–CaO–Al_2O_3–ZrO_2$, $SrO–Al_2O_3$ and $BaO–CaO–Al_2O_3–ZrO_2$ systems were tested. The products formed in the hydration of these binders were detected by SEM-EDS. The linear attenuation coefficients obtained from measurements with γ quanta emitted by the following sources: 22Na, 137Cs, 60Co, 133Ba and 152Eu in the range of 80–1408 keV were determined twice, firstly after casting and drying (110 °C) of concretes, and secondly after sintering at 1400 °C. Especially, this work fills the gap in the literature providing the gamma rays attenuation properties of cement-containing heat-resistant corundum concretes in the energy region between 779 keV and 1112 keV. The experimental setup equipped with the ORTEC GMX25P4-70 High Purity Germanium detector (HPGe) cooled with liquid nitrogen was used for determination of the gamma-ray linear attenuation coefficients of new materials. The role of the cement on the compressive and bending strengths, pore structure (mercury intrusion porosimetry), phase composition (XRD, FT-IR) and microstructure (SEM-EDS) of heat-treated concretes was reported. It was found that the incorporation of Sr or Ba and Zr elements with cements improved the attenuation properties of corundum-based concretes, in comparison to the concretes containing Ca. The doping alkaline earth elements i.e. Sr and Ba were chemically bonded within both hydraulic matrix of green concretes and ceramic matrix formed in concrete through sintering at 1400 °C. Hence, these materials with gamma radiation shielding capacity are designed for special construction applications.

1. Introduction

Concrete, being a construction material composed of cement, both fine and coarse heavy weight aggregates mixed with water which hardens with time, has been used in the construction of nuclear facilities because of two primary advantages, its structural strength and its ability to shield radiation. Several attempts have been made to investigate e.g. the effect of cement and aggregate type and water to cement weight ratio (w/c) on the physical properties, gamma and neutron shielding effectiveness of concretes [1–6]. It has been reported in the recent

Table 1
Batch compositions of castables (wt.%).

Raw materials	Index	Sample code		
		A	B	C
White tabular alumina	0.2–3 mm	55.05	55.05	55.05
Electrocorundum	0–0.1	5.77	5.77	5.77
Reactive aluminas	≥325 mesh	27.18	27.18	27.18
Microsilica	971U	2.00	2.00	2.00
Calcium aluminate cement	G50+	10.00	–	–
Calcium aluminate cement	G70	–	2.73	2.73
Sr-doped CaO–Al$_2$O$_3$–ZrO$_2$ cement	325 mesh	–	5.45	–
SrAl$_2$O$_4$-based cement	325 mesh	–	1.82	–
Ba-doped CaO–Al$_2$O$_3$–ZrO$_2$ cement	325 mesh	–	–	7.27
Dispersant	M-ADS + M-ADW	1.0	1.0	1.0
Water	Distilled	11.0	11.0	11.0

literature that, many efforts have been undertaken to find new concrete having a high resistance against elevated temperature [7–9].

As is well known to those skilled in the concrete technology, the binder choice drives the optimization of overall properties of concrete including engineering, mechanical, structural, and radiation shielding properties. Three well-known strategies for solving these optimization problems are the binder design, the choice of aggregates and the concrete mix design. Portland cements are concerned as the representative binder of commonly used binder for shielding concretes together with other coarse aggregates. Heavy-weight and nuclear-shielding coarse aggregates types are natural mineral and synthetic aggregates. The commonly used types of natural mineral aggregates are boron minerals (colemanite), barium minerals (barite) and iron minerals and ores (hematite, magnetite, limonite). The commonly used types of manufactured synthetic aggregates are boron frit glasses, ferroboron, boron carbide, ferrophosphorus, steel punchings, heavy slags and ferrosilicon [10–11].

With regard to the systematic literature review on hydraulic binders for shielding concrete, the divalent metal aluminate phases and aluminates-containing composite cements seem to have an increasing interest, especially due to their excellent refractory properties. Nowadays, calcium aluminate cements are the only used aluminous cements designed for high performance unshaped refractory materials (monolithic refractories) [12–14]. However, the doping of the calcium aluminate (Ca–Al–O) series with different CaO to Al$_2$O$_3$ proportions with Sr^{2+} or Ba^{2+} ions can predispose these cements to be used as components of radiation shielding ceramic materials [15–18]. It is found that the single-phase solid solutions of Ca$_{1-x}$Sr$_x$Al$_2$O$_4$ exist only over a very limited range, x < 0.35 and x > 0.85 [19]; x = 1 to x = 0.5 [20] or x < 0.25 and x > 0.75 [21]. It was also found that the miscibility between two endmembers CaAl$_2$O$_4$ and BaAl$_2$O$_4$ is incomplete [22]. Two binary solid solution systems with the general formula (Ca,Ba)Al$_2$O$_4$ exist – one on the Ca side yielding Ca rich solid solutions, the other on the Ba side giving rise to Ba rich solid solutions. Many interesting applications of the Ba-bearing compounds in the ceramic technology can be found in [23–26]. These applications include refractory castables based on barium aluminate cements [23–24], engineering ceramics or refractory components containing barium aluminates [25] or refractory concrete containing barium aluminate-barium zirconate cements [26], most of
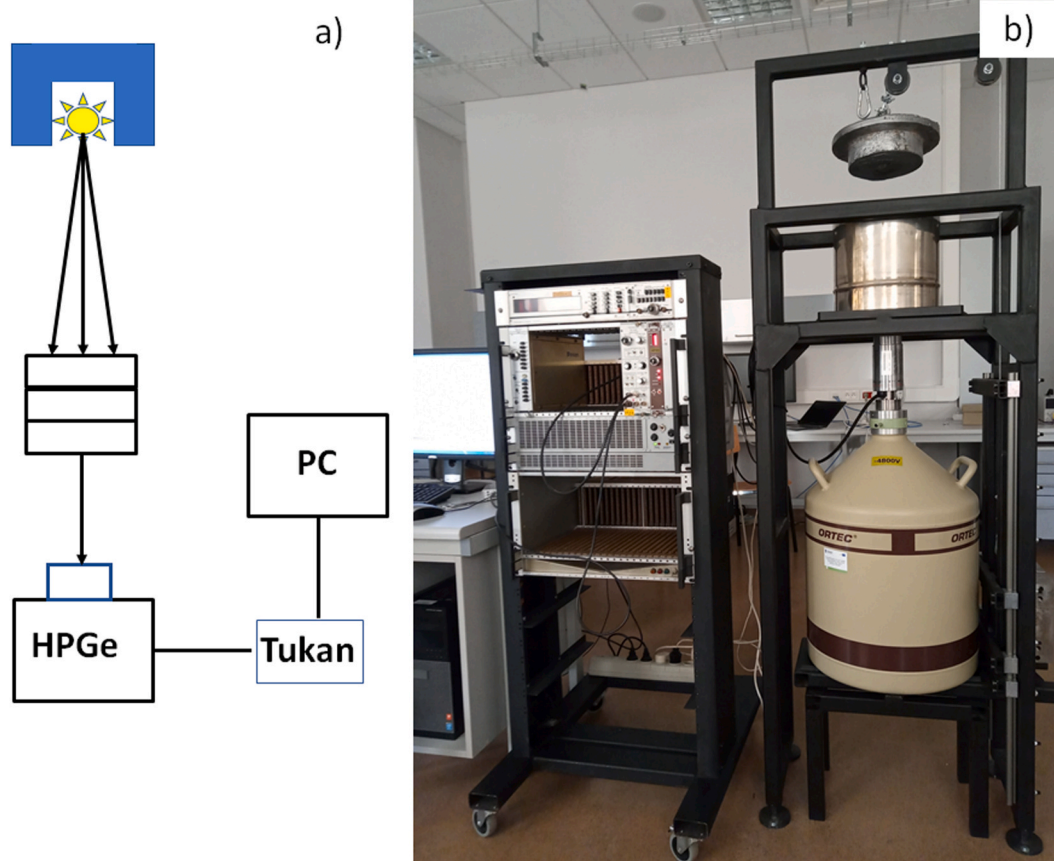

Fig. 1. a) Schematic representation of the experimental setup used in the determination of the linear attenuation coefficients for the studied concretes. An elemental source of γ radiation (yellow star) was collimated with a lead shielding (in blue). Samples of tested material with different thicknesses were placed in front of the ORTEC GMX25P4-70 High Purity Germanium detector (HPGe) [**22**], integrated with a preamplifier, was recording energies of the γ quanta passing through the samples. The Data Acquisition System was composed by the TUKAN multichannel analyzer [**23**] and a computer (PC). b) Photograph of the experimental setup described before. (For interpretation of the references to colour in this figure legend, the reader is referred to the Web version of this article.)
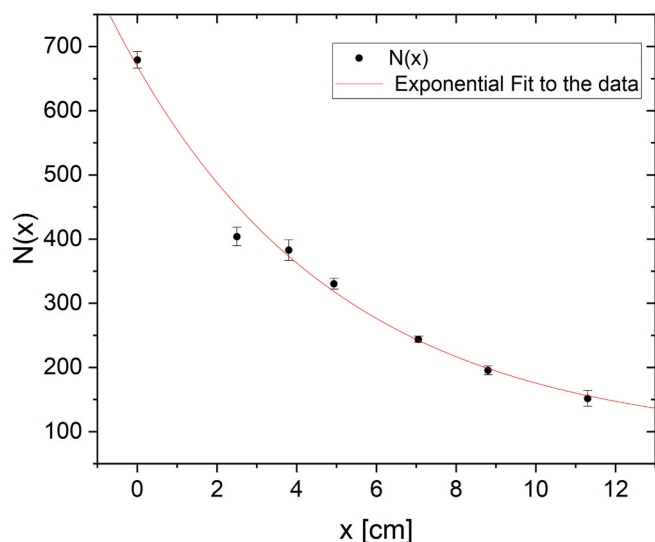
technology of radiation shielding concretes. With going into the details of this issue, the aim of this work is to assess the gamma radiation shielding effectiveness of calcium aluminate cement-containing refractory concretes, and concretes which were additionally doped with strontium or barium. For this purpose, the high purity corundum aggregate was used as a filler together with both commercially available calcium aluminate cements and as-synthesized cements both belonging
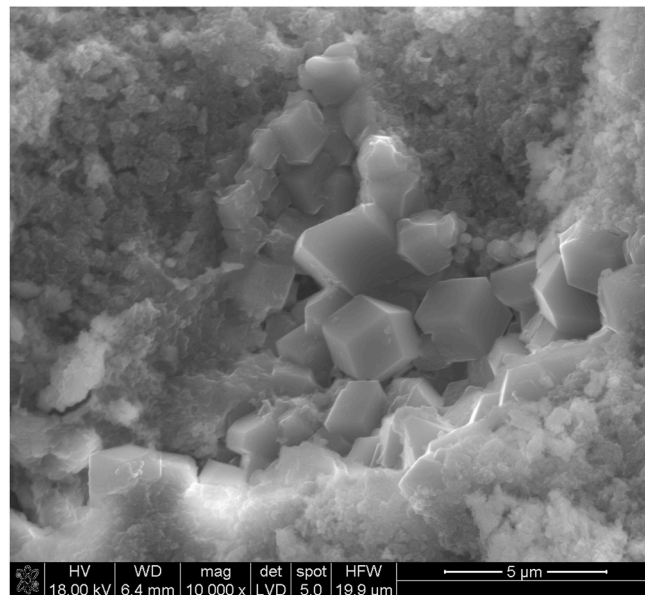
which exhibit gamma ray shielding properties. Recent studies from our laboratory have shown that the Ba^{2+}-, Cu^{2+}- or Bi^{3+}-doped CaO–Al_2O_3–ZrO_2-based cements [27], Sr-doped $Ca_7ZrAl_6O_{18}$ cement [28–30] and $SrAl_2O_4$ [31] cement play a key role in the radiation shielding concretes technology.

With this systematic literature review, we aim to fill gap in providing an implementation of new high-alumina refractory cements in the

Fig. 5. Typical scanning electron microscopy (SEM) image of the microstructure of a 48-h old $SrAl_2O_4$ cement paste.

Fig. 3. Typical scanning electron microscopy (SEM) images of the microstructure of a 48-h old Ba-doped C_7A_3Z cement paste (a and c). Fig. 3b. EDS analysis of the elongated crystals of B-rich (B,C)-A-H hydrates; B = BaO, C = CaO, A = Al_2O_3, H = H_2O.

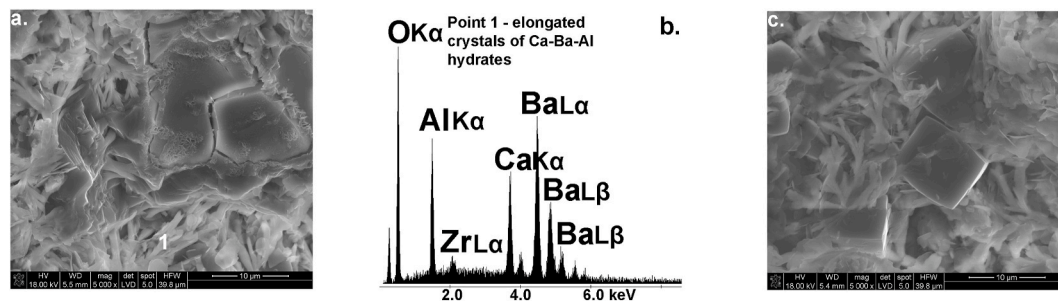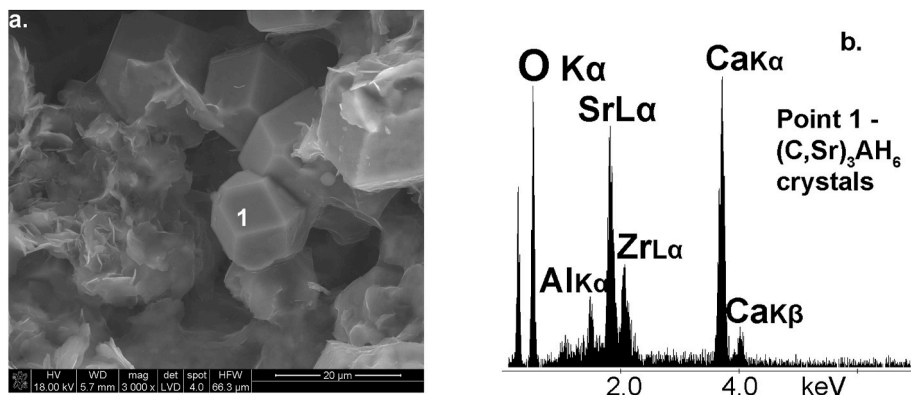**Fig. 4.** Typical scanning electron microscopy (SEM) image of the microstructure of a 48-h old Sr-doped C_7A_3Z cement paste (a). Fig. 4b. EDS analysis of the cubic hydrate Sr-rich $(C,Sr)_3AH_6$; Sr = SrO, C = CaO, A = Al_2O_3, H = H_2O.

◆ Al_2O_3 (JCPDS Card No. 98-007-5559), + $Ca_2Al_2SiO_7$ (JCPDS Card No. 98-002-4588),
° $CaAl_{12}O_{19}$ (JCPDS Card No. 98-020-2616) / $SrAl_{12}O_{19}$ (JCPDS Card No. 98-000-2006)
▽ m-ZrO_2 (JCPDS Card No. 98-006-0900), □ t-ZrO_2 (JCPDS Card No. 98-065-5671)
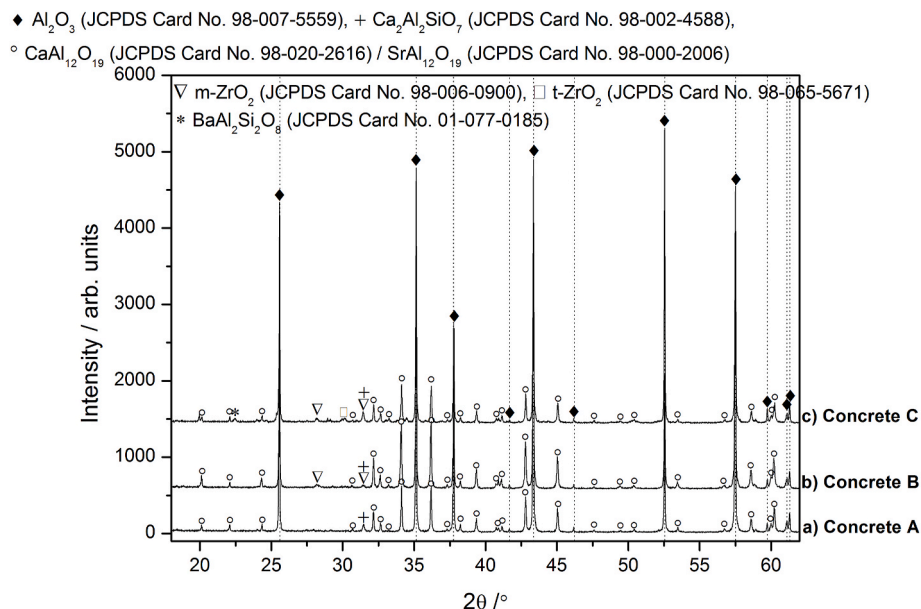* $BaAl_2Si_2O_8$ (JCPDS Card No. 01-077-0185)

Fig. 6. The XRD pattern of the concrete materials A-C after sintering at 1400 °C.

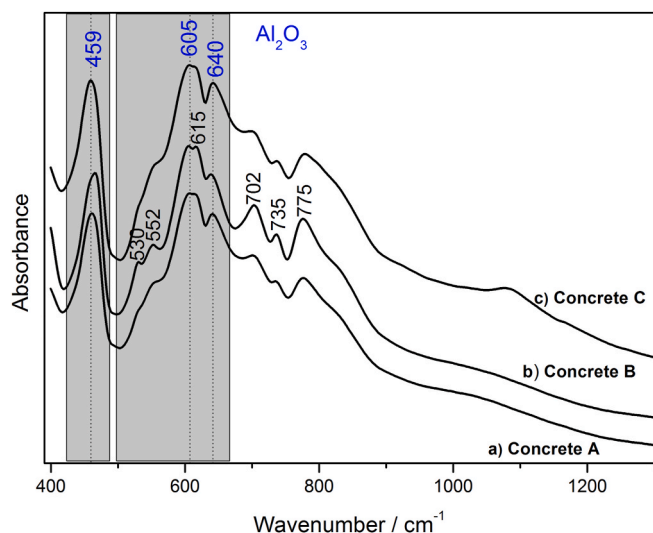**Fig. 7.** FT-IR spectra of the concrete materials A-C after sintering at 1400 °C in the range of 400–4000 cm^{-1}.

to the CaO–Al$_2$O$_3$–ZrO$_2$ system doped with divalent cations Sr or Ba and strontium monoaluminate (SrO·Al$_2$O$_3$) cement.

2. Materials and methods

2.1. Synthesis of Ba-/Sr-doped Ca$_7$ZrAl$_6$O$_{18}$ and SrAl$_2$O$_4$ cements and their hydration characteristics

The preparation of samples with chemical formulas Ca$_{7-x}$Me$_x^{2+}$Z-rAl$_6$O$_{18}$ (where Me^{2+} = Sr^{2+} or Ba^{2+} and x = 1.0) and SrAl$_2$O$_4$ was performed by standard ceramic method. The molecular concentration x is substituted for Sr^{2+} in the chemical formula, as it was presented before [28–30], but x is not substituted for Ba^{2+} in this chemical formula, as it was also presented in Ref. [27]. The oxides Al$_2$O$_3$ and ZrO$_2$ from Acros Organics (with 99.0% purity), and carbonates SrCO$_3$ and BaCO$_3$ from Avantor Performance Materials Poland (with 99.9% purity) were used as starting materials for the synthesis Sr-doped Ca$_7$ZrAl$_6$O$_{18}$, Ba-doped Ca$_7$ZrAl$_6$O$_{18}$ and SrAl$_2$O$_4$ cements. Within each sample, raw materials were calculated and weighted according to the stoichiometric proportion of weight oxides. Three batches of dry powders were homogenized in a laboratory ball mill for 2 h. Then, the resulting powders were pressed at ca. 30 MPa to cylindrical samples of 2 cm in length and diameter, and pre-sintered at 1300 °C for 10 h to get moisture free, homogeneous, calcined samples. The calcined products were hand-crushed, milled to fine powders, pressed into cylinders and then
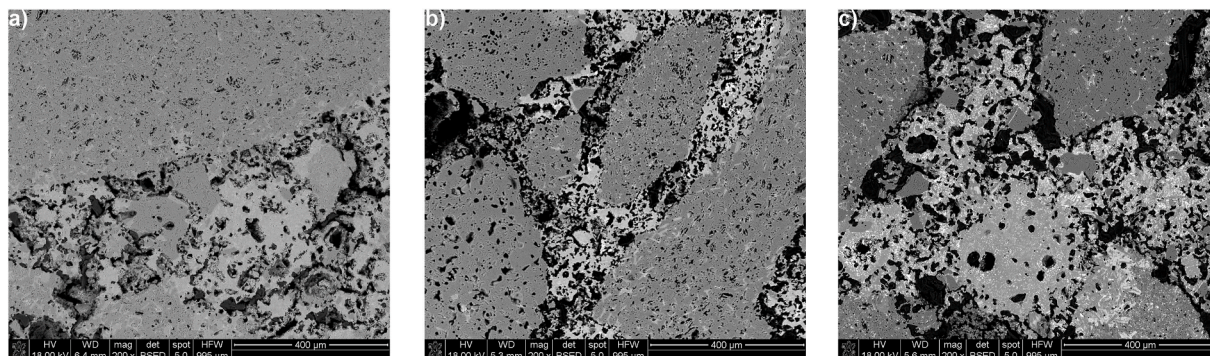

Fig. 8. a–c. An overview of SEM microstructure of concrete material A, B and C.
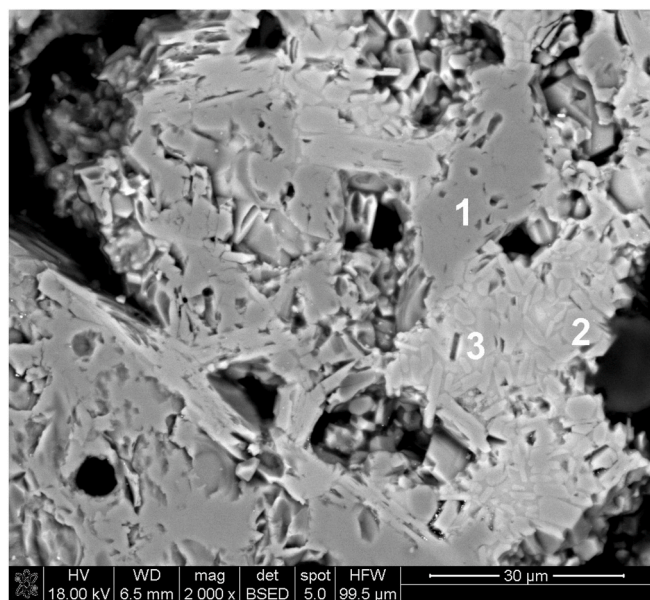
Fig. 9. SEM detailed microstructure of concrete material A. Points 1–3 EDS analysis: 1 – Al_2O_3, 2 – CA_6, and 3 – C_2AS.

sintered at 1400 °C (Sr- or Ba-doped $Ca_7ZrAl_6O_{18}$) or at 1550 °C ($SrAl_2O_4$) in air atmosphere for about 10 h and cooled with the furnace to room temperature. Cement clinkers, which were in the form of small cylinders, were ground to produce finished cements. The commercially available calcium aluminate cements Górkal G50+ and 70 was also used.

The dry cement powders were mixed using water-cement ratio of 1.0 and homogenized cement pastes were casted into polyethylene bags. The neat cement paste samples were conditioned at 50 °C and 90% relative humidity for 48 h. The microstructures of hardened cement pastes were evaluated based on the results of microscopy/chemical analysis of fracture surfaces using SEM-EDS. The hardened cement pastes were pre-treated in an acetone solution to stop the cement hydration and they were checked using XRD.
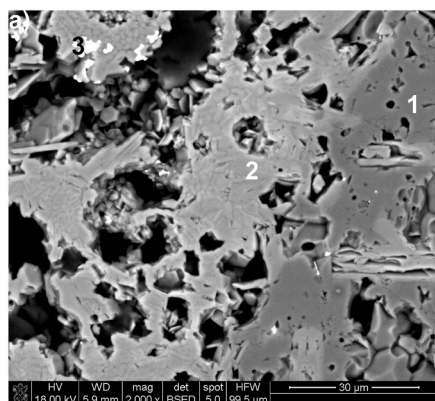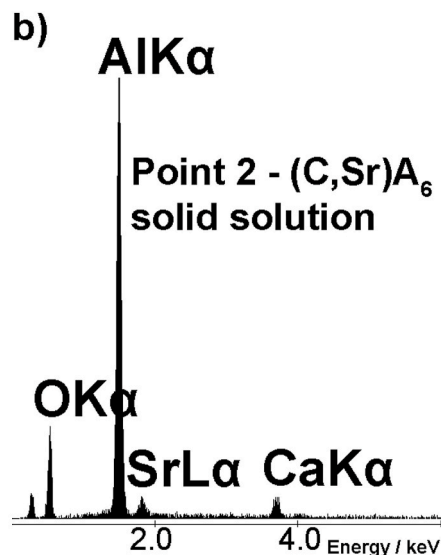
2.2. Concrete materials

Concretes with three different non-traditional aluminate binders alternative to Portland cement were analyzed in this study. For each concrete mixture we used: white tabular alumina (from Almatis) and electrocorundum as grains/aggregates; alumina fines (reactive aluminas from Almatis), microsilica 971U from Elkem, calcium aluminate cement G50+ (Sample A), calcium aluminate cement G70 (Samples B and C) from Górka Cement Sp. z o. o., Sr-doped C_7A_3Z-based and $SrAl_2O_4$ presynthesized cements (Sample B) or Ba-doped C_7A_3Z-based presynthesized cement (Sample C), additives and water (Table 1). After the dry- and wet mixing procedures, two cubic (~50 × 50 × 50 mm and ~70 × 70 × 38 mm) and one prismatic (25 × 25 × 120 mm) samples were cast from each batch, cured at room temperature for 24 h under relative humidity ~95%, dried at 110 °C for another 24 h (green concretes) and finally sintered at 1400 °C for 5 h.

2.3. Testing

X-ray diffraction (XRD) was used to determine the crystalline phases. The XRD patterns were recorded using a X'Pert Pro PANalytical diffractometer within the range of 2θ values between 5° and 90° using Cu Kα radiation (λ = 1.54060 nm) at 45 kV (step size of 0.008°). The X-ray diffraction patterns were compared with JCPDS database. FT-IR spectroscopy was adopted to obtain fundamental information concerning the functional groups of the studied hardened cement pastes and concrete materials. Fourier BIO-RAD FTS60V spectrometer was used for this purpose. Microstructure evaluation of the hardened cement pastes and concrete materials was evaluated using SEM-EDS (the NOVA NANO SEM 200 from FEI Europe Company and EDAX). Bulk density and open porosity of the concrete materials were measured by Archimedes' method according to the polish standard PN-EN 993–1:2019–01. Mercury porosimetry (PoreMaster 60 Quantachrome) was used to determine the internal structure of porous concrete materials. Mechanical properties both cold modulus of rupture (CMOR) and cold crushing strength (CCS) of the sintered concrete materials A, B and C were determined according to the PN-EN 1402–6:2005 and PN-EN ISO 1927–6:2013-06 standards, respectively.

The attenuation of γ quanta by a given absorber can be characterized by a linear or mass attenuation coefficient which in general is dependent on the energy of photons. The intensity of γ quanta beam after passing by an absorber of thickness x can be expressed as Lamberts law:

Fig. 10. a SEM detailed microstructure of concrete material B. Points 1–3 EDS analysis: 1 – Al_2O_3, 2 – $(C,Sr)A_6$ solid solution and 3 – ZrO_2. Fig. 10b. Representative EDS spectrum of light grey regions (Point 2 – $(C,Sr)A_6$ solid solution) surrounding coarse alumina grain in Fig. 10a.
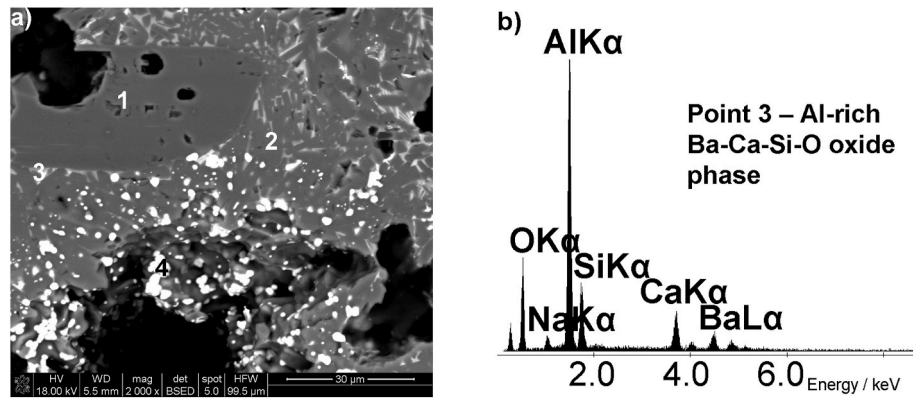
Fig. 11. a SEM detailed microstructure of concrete material C. Points 1–4 EDS analysis: 1 – Al_2O_3, 2 – CA_6, 3 – Al-rich Ba–Ca–Si–O oxide inclusion, and 4 – ZrO_2. Fig. 11b. Representative EDS spectrum of light grey regions (Point 3 – Al-rich Ba–Ca–Si–O oxide phase) surrounding needle-shaped crystals of CA_6 in Fig. 11a.

Table 2
Elemental analysis of concrete materials before sintering.

Sample	Element									Total
	Al	Ca	Ba	Sr	Fe	Si	Zr	O	H	
	Component/mass %									
Concrete A	46.84	2.57	–	–	0.20	1.06	–	48.75	0.58	100
Concrete B	46.47	1.59	–	1.18	–	0.89	0.55	48.74	0.58	100
Concrete C	46.28	2.32	1.04	–	–	0.89	0.69	48.20	0.58	100

Table 3
Elemental analysis of concrete materials sintered at 1400 °C.

Sample	Element								Total
	Al	Ca	Ba	Sr	Fe	Si	Zr	O	
	Component/mass %								
Concrete A	49.41	2.72	–	–	0.22	1.12	–	46.53	100
Concrete B	49.02	2.14	–	1.24	–	0.72	0.58	46.30	100
Concrete C	48.82	2.44	1.09	–	–	0.72	0.73	46.20	100

Table 4
Physical and mechanical properties of concrete materials sintered at 1400 °C.

Concrete	Density/g cm^{-3}	Open porosity/%	CMOR/MPa	CCS/MPa
A	2.79	24.4	34.8	114.9
B	2.72	26.4	31.1	89.6
C	2.64	28.5	25.2	77.8

$$N(x) = N_0 e^{-\mu x} \tag{1}$$

where μ is the linear attenuation coefficient and N_0 denotes the initial intensity of the beam hitting the absorber. Thus, one of the possible way to determine the attenuation properties (μ) of a new material are measurements of the number of γ quanta passing through the absorber without any interactions in a function of its thickness. In such a measurements one usually uses elemental sources providing γ quanta with well-defined energies (e.g. 22Na or 137Cs). A scheme of the experimental setup used in characterization of the materials presented in this article is shown in Fig. 1a.

Since the shielding properties against gamma quanta characterizing any material in general depends on energy of the radiation we have studied photons of energy in the range of 80–1408 keV.

For each sample we have investigated attenuation properties using γ quanta emitted by the following sources: 22Na, 137Cs, 60Co, 133Ba and 152Eu. Each source was placed in a led collimator which at the same

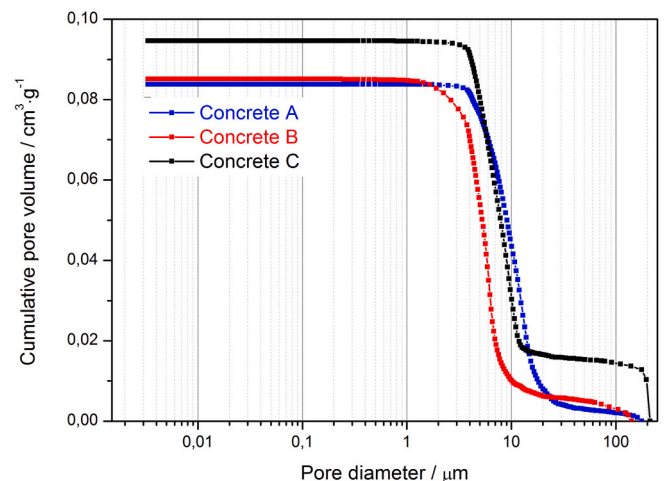**Fig. 12.** Cumulative pore volume as a function of the pore diameter of the concrete materials A-C after sintering at 1400 °C.

time served as a shielding material against the environmental radiation background. For precise determination of the attenuation coefficient we have used the ORTEC GMX25P4-70 High Purity Germanium detector (HPGe) cooled with liquid nitrogen (see Fig. 1b). It provides excellent
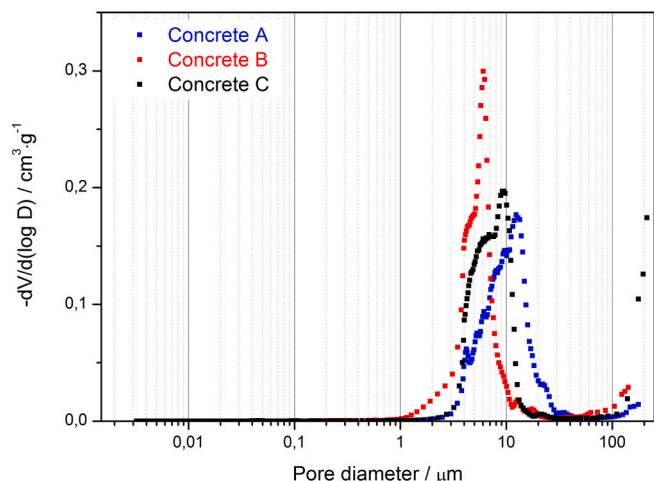
Fig. 13. Log differential volume −dV/d(log d) versus pore diameter of the concrete materials A-C after sintering at 1400 °C.

energy resolution, 1.90 keV at 1330 keV line, and peak to Compton ratio of 53:1 [32] which are crucial in the precise determination of the number of γ quanta passing through the sample without interaction. Each studied sample was placed inside the led shield between the surface of the detector and collimated source. The detector was registering the γ quanta passing through the sample and measuring their energies. For each energy line we have determined the net counts by fitting the Gaussian function and integrating the peak area within the range of ±3σ [33] around the central value. Such measurements were done without any sample and for several samples of different thickness for each studied concrete within a fixed time interval of 1000 s. An example of the net counts dependence on the sample thickness obtained for concrete B at 152Eu line of energy 1408 keV is shown in Fig. 2. A fit of the theoretical curve according to Eq. (1) led to determination of the linear attenuation coefficient μ of the studied concretes at 18 γ quanta energies

up to 1408 keV. Transforming Eq. (1) to the following form:

$$ln\left(\frac{N(x)}{N_0}\right) = -\mu x \tag{2}$$

results in a linear dependence on the absorber thickness and may be also used to determine the value of μ. We have performed an independent analysis of the gathered data using Eq. (2) to check a possible bias on the obtained linear attenuation coefficient values due to the chosen fitting method. The linear attenuation coefficients may be used to determine other quantities relevant to the radiation protection, like the Half-Value Layer (the average amount of material needed to reduce the radiation intensity by 50%): $HVL = \frac{\ln(2)}{\mu}$. Knowing the density of each sample, ρ, one can estimate also the mass attenuation coefficient $\mu_m = \mu/\rho$ which opens possibility to estimate the effective atomic number of the tested concretes and the total atomic cross section [34]:

$$\sigma_a = \frac{\mu_m}{N_a \sum_i w_i/A_i} \tag{3}$$

where N_a denotes the Avogadro number, w_i is the proportion by weight of the material's ith constituent element and A_i stands for its atomic weight.

3. Results

3.1. AS-SYNTHESIZED cement clinkers

Three aluminate-based cement clinkers Ba-doped $Ca_7ZrAl_6O_{18}$, Sr-doped $Ca_7ZrAl_6O_{18}$ and $SrAl_2O_4$ clinkers were successfully synthesized via a two-step ceramic route through calcination and sintering. The Ba-doped C_7A_3Z clinker contains one major ($Ca_7ZrAl_6O_{18}$) and two minor constituents ($Ba_{0.8}Ca_{0.2}ZrO_3$, $BaAl_2O_4$) as presented in Ref. [27], whereas the $(Sr,Ca)_7ZrAl_6O_{18}$ solid solution exists as the main constituent of the Sr-doped C_7A_3Z clinker with some admixture of $(Ca,Sr)ZrO_3$ phase [28–30]. Going into details, the XRD patterns of as-synthesized Ba-doped $Ca_7ZrAl_6O_{18}$ and Sr-doped $Ca_7ZrAl_6O_{18}$ powders were in
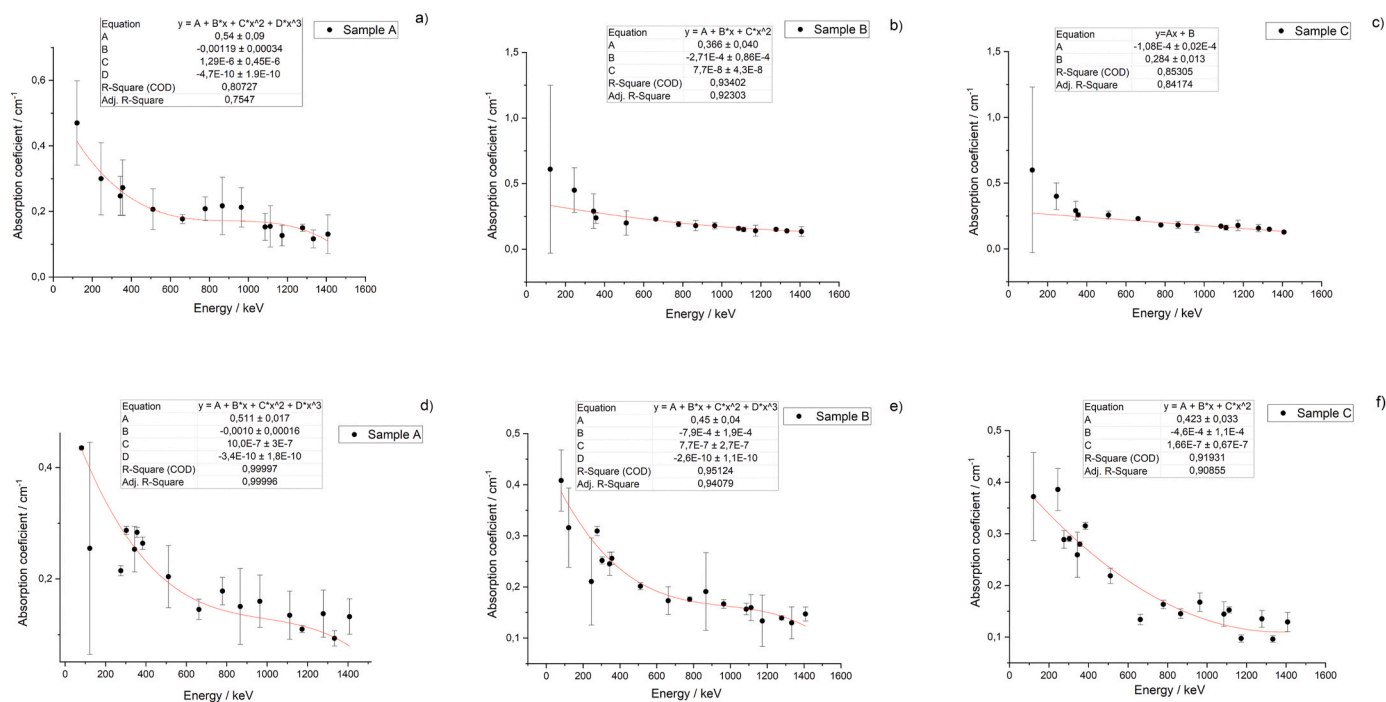
Fig. 14. Linear attenuation coefficients obtained from measurements with γ quanta in the range of 80–1408 keV for all the concretes presented in this paper before (a–c) and after sintering (d–f). The error bars represent both the statistical and systematic uncertainties added in quadrature. For each spectrum the red curve represent polynomial fit do the data. (For interpretation of the references to colour in this figure legend, the reader is referred to the Web version of this article.)

Table 5
Values of the mass attenuation coefficients and Half-Value Layer (the average amount of material needed to reduce the radiation intensity by 50%) as a function of gamma quanta energies obtained for concrete materials before sintering.

Energy/ keV	SAMPLE A		SAMPLE B		SAMPLE C	
	μ_m/cm²/g	HVL/ cm	μ_m/cm²/g	HVL/ cm	μ_m/cm²/g	HVL/ cm
122	0.168 ± 0.046	1.47 ± 0.19	–	–	–	–
245	0.108 ± 0.039	2.31 ± 0.25	0.165 ± 0.063	1.54 ± 0.26	0.152 ± 0.038	1.73 ± 0.17
344	0.089 ± 0.021	2.80 ± 0.17	0.107 ± 0.048	2.39 ± 0.31	0.110 ± 0.027	2.39 ± 0.17
356	0.098 ± 0.030	2.55 ± 0.21	0.088 ± 0.015	2.91 ± 0.12	0.098 ± 0.006	2.69 ± 0.04
511	0.074 ± 0.022	3.36 ± 0.21	0.074 ± 0.034	3.47 ± 0.32	0.097 ± 0.011	2.70 ± 0.08
662	0.063 ± 0.005	3.92 ± 0.05	0.084 ± 0.004	3.02 ± 0.04	0.087 ± 0.002	3.02 ± 0.02
779	0.075 ± 0.013	3.33 ± 0.12	0.070 ± 0.007	3.63 ± 0.07	0.069 ± 0.002	3.81 ± 0.02
867	0.078 ± 0.031	3.19 ± 0.28	0.066 ± 0.014	3.85 ± 0.15	0.069 ± 0.010	3.81 ± 0.10
964	0.076 ± 0.022	3.26 ± 0.2	0.066 ± 0.009	3.86 ± 0.09	0.059 ± 0.011	4.49 ± 0.13
1086	0.055 ± 0.015	4.55 ± 0.19	0.058 ± 0.005	4.38 ± 0.07	0.065 ± 0.002	4.02 ± 0.02
1112	0.055 ± 0.023	4.48 ± 0.28	0.055 ± 0.006	4.61 ± 0.08	0.061 ± 0.007	4.30 ± 0.08
1173	0.045 ± 0.011	5.48 ± 0.17	0.052 ± 0.016	4.90 ± 0.21	0.068 ± 0.015	3.87 ± 0.16
1278	0.054 ± 0.004	4.63 ± 0.05	0.055 ± 0.004	4.60 ± 0.05	0.059 ± 0.010	4.42 ± 0.12
1333	0.042 ± 0.010	5.96 ± 0.16	0.052 ± 0.002	4.94 ± 0.03	0.056 ± 0.003	4.65 ± 0.03
1408	0.047 ± 0.021	5.31 ± 32	0.050 ± 0.014	5.13 ± 0.19	0.048 ± 0.002	5.43 ± 0.03

Table 6
Values of the total atomic cross sections and effective atomic numbers as a function of gamma quanta energies obtained for concrete materials before sintering.

Energy/ keV	SAMPLE A		SAMPLE B		SAMPLE C	
	σ_a/b/ atom	Z_{eff}	σ_a/b/ atom	Z_{eff}	σ_a/b/ atom	Z_{eff}
122	5.1 ± 1.4	10.3 ± 2.5	–	–	–	–
245	3.3 ± 1.2	8.5 ± 3.0	5.1 ± 1.9	13.0 ± 4.5	4.7 ± 1.2	12.0 ± 2.8
344	2.69 ± 0.65	8.0 ± 1.8	3.3 ± 1.5	9.6 ± 4.3	3.37 ± 0.83	10.0 ± 2.3
356	2.96 ± 0.92	8.9 ± 2.6	2.68 ± 0.46	8.1 ± 1.5	3.00 ± 0.18	9.0 ± 0.6
511	2.25 ± 0.68	7.8 ± 2.2	2.3 ± 1.1	7.8 ± 3.5	2.98 ± 0.35	10.4 ± 1.2
662	1.93 ± 0.15	7.5 ± 0.6	2.57 ± 0.13	10.0 ± 0.5	2.67 ± 0.07	10.4 ± 0.3
779	2.27 ± 0.40	9.5 ± 1.6	2.14 ± 0.22	9.0 ± 2.4	2.11 ± 0.06	8.7 ± 0.6
867	2.36 ± 0.95	10.4 ± 4.2	2.02 ± 0.43	8.9 ± 1.8	2.12 ± 0.31	9.3 ± 1.4
964	2.31 ± 0.65	10.7 ± 2.9	2.01 ± 0.28	9.4 ± 1.3	1.80 ± 0.34	8.4 ± 1.6
1086	1.66 ± 0.45	8.2 ± 2.3	1.78 ± 0.17	8.8 ± 0.8	2.01 ± 0.06	9.9 ± 0.3
1112	1.68 ± 0.69	8.4 ± 3.5	1.69 ± 0.20	8.4 ± 1.0	1.87 ± 0.22	9.3 ± 1.4
1173	1.38 ± 0.34	7.0 ± 1.9	1.59 ± 0.47	8.1 ± 2.5	2.08 ± 0.47	10.6 ± 2.4
1278	1.63 ± 0.12	8.7 ± 0.6	1.69 ± 0.11	9.0 + 0.6	1.82 ± 0.32	9.8 ± 1.6
1333	1.27 ± 0.30	6.9 ± 1.5	1.57 ± 0.07	8.6 ± 0.4	1.73 ± 0.08	9.2 ± 0.2
1408	1.42 ± 0.65	8.0 ± 8.0	1.52 ± 0.41	8.5 ± 2.3	1.48 ± 0.06	8.4 ± 0.4

agreement with JCPDS Card No. 98-018-2622 with slight peak shifts towards lower angles, which is believed to be caused by the presence of Ba and Sr doping element in solid solutions in $Ca_7ZrAl_6O_{18}$, respectively. We also found that strontium ions more readily dissolve into $Ca_7ZrAl_6O_{18}$ crystal lattice than barium ions. With respect to the as-synthesized strontium aluminate clinker, the XRD pattern indicates an almost single phase sample of $SrAl_2O_4$ according to the JCPDS Card No. 98-002-6466.

In commercially available calcium aluminate cements, there were many mineralogical phases present in the G50+ cement i.e. calcium monoaluminate CA as a main phase (JCPDS Card No. 98-018-0997), calcium dialuminate CA_2 (JCPDS Card No. 00-046-1475), brownmillerite C_4AF (JCPDS Card No. 98-002-7112), dodecacalcium heptaaluminate $C_{12}A_7$ (JCPDS Card No. 98-000-6287), gehlenite C_2AS (JCPDS Card No. 98-016-0331) as secondary phases; in the G70 cement i.e. CA, CA_2 as main phases, and $C_{12}A_7$, α-Al_2O_3 (JCPDS Card No. 98-009-9783) as secondary phases.

3.2. Hardened cement pastes

Three types of as-synthesized aluminate-based cement clinkers were ground and finally, the fine powdered cements were mixed with water to obtain the neat cement pastes. Morphological features of hydrated cement pastes exhibited on carefully fractured and carbon coated fracture surfaces have been critically examined using SEM/EDS. The results of scanning electron microscopy (SEM) analysis of morphological characteristics of the Ba-doped or Sr-doped $Ca_7ZrAl_6O_{18}$ and $SrAl_2O_4$ cement pastes prepared at a water-to-solid weight ratio of 1.0 at the age of 48 h are presented in Figs. 3–5, respectively. The hydration characteristics were observed mainly by changes in the C-(Ba^{2+} or Sr^{2+})-A-H and Sr-A-H phases (Figs. 3–5). It can be observed, that there is a residual

core of the unhydrated Ba-doped C_7A_3Z cement surrounded by the elongated crystals of calcium-barium-aluminate hydrates (Fig. 3a–b). Fig. 3b shows the EDS spectrum of these elongated crystals containing multiple elements including Ca, Ba, Al and O. Moreover, a barium analogue of hydrogarnet ($Ca_3Al_{12}(OH)_{12}$) i.e. the equidimensional crystals of tribarium aluminate hexahydrate ($Ba_3AI_{12}(OH)_{12}$) or its solid solutions were found (Fig. 3c) [35–48].

Typical SEM image of the microstructure of a 48-h old Sr-doped C_7A_3Z cement paste is presented in Fig. 4. Most of the Sr-doped C_3AH_6 crystals formed at 48-day of hydration attain the shape of cubes, pyritohedra or other more complex forms of the isometric system (Fig. 4b), which are reinforced with small feather-like crystals of calcium-aluminate hydrates, mainly C_4AH_{19} [29].

The microstructure of a 48-h old $SrAl_2O_4$ cement paste is seen to consist of Sr_3AH_6 hydrates, which are reinforced with $Al(OH)_3$ (Fig. 5).

3.3. Concrete materials

3.3.1. XRD, FT-IR and SEM-EDS characterizations of concretes

Regarding to concrete samples A, B and C after sintering at 1400 °C, X-ray diffraction was employed to characterize the phase composition. FT-IR spectroscopy was used to identify the main functional groups of aluminates from concrete samples, whereas SEM-EDS was able to characterize the microstructure of concrete specimens containing various modifiers.

The X-ray diffraction patterns of the concrete materials prepared by the casting and heat treatment after casting and sintered at 1400 °C for 5 h are shown in Fig. 6. As this class of concrete materials was bonded with calcium aluminate cement, the XRD diffraction patterns showed the evidence of the presence of majority of crystalline phases of alumina (Al_2O_3; JCPDS Card No. 98-007-5559) and calcium hexaluminate ($CaAl_{12}O_{19}$; JCPDS Card No. 98-020-2616) in all the investigated

Table 7
Values of the mass attenuation coefficients and Half-Value Layer (the average amount of material needed to reduce the radiation intensity by 50%) as a function of gamma quanta energies obtained for concrete materials after sintering.

Energy/ keV	SAMPLE A μ_m/cm²/g	HVL/ cm	SAMPLE B μ_m/cm²/g	HVL/ cm	SAMPLE C μ_m/cm²/g	HVL/ cm
81	0.156 ± 0.001	1.59 ± 0.01	0.150 ± 0.022	1.70 ± 0.1	–	–
122	0.091 ± 0.068	2.72 ± 0.52	0.116 ± 0.028	2.19 ± 0.17	0.141 ± 0.032	1.86 ± 0.16
245	–	–	0.077 ± 0.031	3.29 ± 0.28	0.146 ± 0.015	1.80 ± 0.07
276	0.077 ± 0.003	3.23 ± 0.03	0.114 ± 0.003	2.24 ± 0.02	0.109 ± 0.006	2.40 ± 0.04
303	0.103 ± 0.003	2.41 ± 0.02	0.093 ± 0.003	2.75 ± 0.02	0.110 ± 0.002	2.39 ± 0.01
344	0.091 ± 0.015	2.74 ± 0.11	0.090 ± 0.008	2.83 ± 0.06	0.098 ± 0.017	2.67 ± 0.12
356	0.102 ± 0.003	2.44 ± 0.02	0.094 ± 0.004	2.71 ± 0.03	0.106 ± 0.002	2.48 ± 0.01
384	0.095 ± 0.004	2.63 ± 0.03	–	–	0.119 ± 0.003	2.20 ± 0.01
511	0.073 ± 0.020	3.40 ± 0.19	0.074 ± 0.003	3.44 ± 0.02	0.083 ± 0.006	3.17 ± 0.05
662	0.052 ± 0.007	4.77 ± 0.09	0.064 ± 0.010	4.00 ± 0.11	0.051 ± 0.004	5.18 ± 0.05
779	0.064 ± 0.009	3.89 ± 0.10	0.065 ± 0.002	3.94 ± 0.02	0.062 ± 0.003	4.25 ± 0.03
867	0.054 ± 0.024	4.61 ± 0.31	0.070 ± 0.028	3.63 ± 0.28	0.055 ± 0.003	4.77 ± 0.04
964	0.057 ± 0.017	4.34 ± 0.20	0.061 ± 0.003	4.16 ± 0.04	0.063 ± 0.007	4.14 ± 0.07
1086	–	–	0.058 ± 0.004	4.42 ± 0.05	0.055 ± 0.009	4.79 ± 0.11
1112	0.048 ± 0.015	5.15 ± 0.22	0.059 ± 0.009	4.35 ± 0.11	0.058 ± 0.002	4.55 ± 0.03
1173	0.039 ± 0.002	6.30 ± 0.04	0.049 ± 0.018	5.19 ± 0.26	0.037 ± 0.003	7.13 ± 0.05
1278	0.049 ± 0.015	5.04 ± 0.21	0.051 ± 0.002	4.98 ± 0.02	0.051 ± 0.006	5.13 ± 0.08
1333	0.033 ± 0.005	7.42 ± 0.10	0.048 ± 0.011	5.34 ± 0.17	0.036 ± 0.002	7.21 ± 0.05
1408	0.047 ± 0.011	5.23 ± 0.17	0.054 ± 0.005	4.72 ± 0.06	0.049 ± 0.007	5.37 ± 0.10

Table 8
Values of the total atomic cross sections and effective atomic numbers as a function of gamma quanta energies obtained for concrete materials after sintering.

Energy/ keV	SAMPLE A σ_a/b/ atom	Z_{eff}	SAMPLE B σ_a/b/ atom	Z_{eff}	SAMPLE C σ_a/b/ atom	Z_{eff}
81	5.34 ± 0.04	9.3 ± 0.1	5.18 ± 0.76	9.0 ± 1.0	–	–
122	3.1 ± 2.3	6.6 ± 4.6	4.0 ± 1.0	8.3 ± 1.9	4.86 ± 1.1	10.0 ± 2.0
245	–	–	2.7 ± 1.1	7.0 ± 2.6	5.04 ± 0.53	13.0 ± 1.2
276	2.63 ± 0.11	7.2 ± 0.3	3.93 ± 0.11	10.7 ± 0.3	3.78 ± 0.22	10.3 ± 0.6
303	3.52 ± 0.09	9.9 + 0.2	3.20 ± 0.10	13.0 ± 0.3	3.80 ± 0.07	10.7 ± 0.2
344	3.11 ± 0.50	10.0 ± 2.0	3.10 ± 0.30	10.6 ± 1.1	3.39 ± 0.57	10.0 ± 1.7
356	3.48 ± 0.11	11.4 ± 0.1	3.25 ± 0.15	11.1 ± 0.2	3.66 ± 0.06	11.6 ± 0.1
384	3.24 ± 0.13	10.0 ± 0.4	–	–	4.12 ± 0.09	12.7 ± 0.3
511	2.50 ± 0.68	8.7 ± 2.3	2.6 ± 0.1	8.9 ± 0.3	2.90 ± 0.20	9.9 ± 0.6
662	1.78 ± 0.23	7.0 ± 0.8	2.20 ± 0.35	8.6 ± 1.3	1.75 ± 0.13	6.8 ± 0.5
779	2.19 ± 0.30	9.2 ± 1.3	2.23 ± 0.06	9.4 ± 0.2	2.13 ± 0.11	9.0 ± 0.4
867	1.85 ± 0.84	8.1 ± 3.8	2.4 ± 1.0	10.7 ± 4.2	1.90 ± 0.12	8.4 ± 0.5
964	1.96 ± 0.57	9.1 ± 2.8	2.12 ± 0.11	9.8 ± 0.5	2.19 ± 0.23	10.2 ± 1.1
1086	–	–	1.99 ± 0.14	9.8 ± 0.7	1.89 ± 0.31	9.3 ± 1.6
1112	1.65 ± 0.53	8.2 ± 2.7	2.02 ± 0.32	10.5 ± 1.7	1.99 ± 0.08	9.9 ± 0.4
1173	1.35 ± 0.08	6.9 ± 0.4	1.70 ± 0.64	8.7 ± 3.2	1.30 ± 0.10	6.5 ± 0.5
1278	1.69 ± 0.52	9.0 ± 3.0	1.77 ± 0.05	9.5 ± 0.3	1.77 ± 0.21	9.5 ± 1.1
1333	1.15 ± 0.17	6.3 ± 1.0	1.70 ± 040	9.0 ± 2.3	1.26 ± 0.08	6.9 ± 0.4
1408	1.62 ± 0.39	9.1 ± 2.3	1.87 ± 0.17	10.5 ± 1.0	1.69 ± 0.24	9.5 ± 1.3

samples. As two concrete materials were additionally bonded with Sr-doped $Ca_7ZrAl_6O_{18}$ and $SrAl_2O_4$ cements (Sample B), or Ba-doped $Ca_7ZrAl_6O_{18}$ cement (Sample C), many different secondary phases were formed. As the Sr-doped $Ca_7ZrAl_6O_{18}$ and $SrAl_2O_4$ cements were added into the concrete material B, calcium and strontium hexaaluminates $MAl_{12}O_{19}$ (M = Ca, Sr) were observed rather than "pure, undoped" $CaAl_{12}O_{19}$ (Fig. 6b). Thus, as the results in Fig. 6a and 6b–c are compared, the reactions between hydrated $Ca_7ZrAl_6O_{18}$ and the alumina lead to the formation of Zr-containing secondary phases besides the hexaluminates in the concrete materials B and C which is in qualitative agreement with experimental observations of Madej et al. [49–50]. Moreover, the reactions between calcia and alumina from cements, and microsilica result in formation of gehlenite ($Ca_2Al_2SiO_7$; JCPDS Card No. 98-002-4588) as a secondary phase (Fig. 6a–c) and the reaction between barium, silica and alumina result in formation of barium aluminum silicate ($BaAl_2Si_2O_8$; JCPDS Card No. 01-077-0185) (Fig. 6c).

Absorption spectra in the range from 1300 to 400 cm^{-1} of the concrete materials A, B and C prepared by the casting and heat treatment and sintering at 1400 °C for 5 h are presented in Fig. 7. Two main absorption ranges: 900-500 cm^{-1} and 500-420 cm^{-1} can be distinguished in the infrared absorption spectra of these systems. The first range contains strong absorption band centered at ca. 459 cm^{-1} due to isolated AlO_6 octahedra in alumina [51]. The most characteristic feature of all

spectra is the occurrence of two strong band near 640 and 605 cm^{-1} due to condensed AlO_6 octahedra in alumina. The bands belonging to hexaaluminates between ca. 900-700 cm^{-1} and 700-400 cm^{-1} correspond to AlO_6 and AlO_4 vibrations, respectively [52–54]. The maximum peaks were located at ca. 530, 552, 615, 702, 735 and 775 cm^{-1}, which are in very good agreement with the spectra presented elsewhere [49]. The peaks at ca. 735 cm^{-1} probably also belongs to the m-ZrO_2 [55].

Generally, it can be stated that all the investigated concretes have a heterogenous microstructure, which consists of four main components, namely coarse aggregates, ceramic matrix containing binder and fine particles, interfacial transition zone between the matrix and aggregates, and pore structure (Fig. 8a–c). It can be seen from an overview of SEM microstructure of each concrete material presented in Fig. 8a–c, that numerous light grey phases are uniformly distributed in the porous matrix that surrounds the alumina aggregate particles. At higher magnification and after the EDS analysis, as shown in Fig. 9, **10a** and **11a**, it is clear that the light grey matrix mainly consists of CA_6, Al_2O_3 and C_2AS (concrete A, Fig. 9); (C,Sr)A_6 solid solution, Al_2O_3 and ZrO_2 (concrete B, Fig. 10a); Al_2O_3, CA_6, ZrO_2, C_2AS and Ba–Ca–Si–Al–O oxide inclusion (concrete C, Fig. 11a).

3.3.2. Chemical, physical and mechanical properties of concretes

The chemical composition of concretes before and after sintering at 1400 °C is presented in Table 2 and Table 3, respectively.

The physical and mechanical properties including density and open

Table 9
Comparison of the mass attenuation coefficients obtained for concrete C after sintering with the shielding properties of gas concrete [58], WO$_3$ doped concrete [9], Lead-flyash concrete [10] and cement [58].

μ_m/cm^2/g

Energy/keV	Concrete C (sintered)	Gas concrete	WO$_3$ doped concrete	Lead-flyash concrete	Turkey Cement
122	0.141 ± 0.032	0.180 ± 0.012	–	–	0.172 ± 0.011
245	0.146 ± 0.015	–	–	–	–
276	0.109 ± 0.006	0.125 ± 0.009	0.056 ± 0.003	–	0.112 ± 0.008
303	0.110 ± 0.002	0.111 ± 0.007	0.054 ± 0.003	–	0.106 ± 0.007
344	0.098 ± 0.017	–	–	–	–
356	0.106 ± 0.002	0.098 ± 0.007	0.049 ± 0.003	–	0.100 ± 0.006
384	0.119 ± 0.003	0.098 ± 0.006	0.044 ± 0.003	–	0.097 ± 0.006
511	0.083 ± 0.006	0.082 ± 0.005	–	–	0.086 ± 0.006
662	0.051 ± 0.004	0.070 ± 0.005	–	0.0840 ± 0.0018	0.076 ± 0.005
779	0.062 ± 0.003	–	–	–	–
867	0.055 ± 0.003	–	–	–	–
964	0.063 ± 0.007	–	–	–	–
1086	0.055 ± 0.009	–	–	–	–
1112	0.058 ± 0.002	–	–	–	–
1173	0.037 ± 0.003	0.055 ± 0.004	–	0.0586 ± 0.0011	0.059 ± 0.004
1278	0.051 ± 0.006	0.048 ± 0.003	–	–	0.056 ± 0.004
1333	0.036 ± 0.002	0.045 ± 0.003	–	0.0553 ± 0.0014	0.052 ± 0.003
1408	0.049 ± 0.007	–	–	–	–

Table 10
Comparison of the total atomic cross sections and effective atomic numbers obtained for concrete C after sintering with similar materials studied in Ref. [58].

Energy/keV	SAMPLE C (sintered)		Turkey Cement		Gas Concrete	
	σ$_a$/b/atom	Z_{eff}	σ$_a$/b/atom	Z_{eff}	σ$_a$/b/atom	Z_{eff}
122	4.86 ± 1.1	10.0 ± 2.0	6.68 ± 0.43	12.81 ± 0.86	6.73 ± 0.44	12.51 ± 0.90
245	5.04 ± 0.53	13.0 ± 1.2	–	–	–	–
276	3.78 ± 0.22	10.3 ± 0.6	4.35 ± 0.33	11.77 ± 0.75	4.67 ± 0.33	12.61 ± 0.93
303	3.80 ± 0.07	10.7 ± 0.2	4.12 ± 0.26	11.54 ± 0.79	4.15 ± 0.28	11.63 ± 0.91
344	3.39 ± 0.57	10.0 ± 1.7	–	–	–	–
356	3.66 ± 0.06	11.6 ± 0.1	3.88 ± 0.28	11.62 ± 0.90	3.66 ± 0.27	10.98 ± 0.74
384	4.12 ± 0.09	12.7 ± 0.3	3.77 ± 0.25	11.61 ± 0.84	3.66 ± 0.26	11.29 ± 0.78
511	2.90 ± 0.20	9.9 ± 0.6	3.34 ± 0.26	11.60 ± 0.75	3.07 ± 0.20	10.65 ± 0.74
662	1.75 ± 0.13	6.8 ± 0.5	2.95 ± 0.19	11.48 ± 0.77	2.62 ± 0.19	10.19 ± 0.63
779	2.13 ± 0.11	9.0 ± 0.4	–	–	–	–
867	1.90 ± 0.12	8.4 ± 0.5	–	–	–	–
964	2.19 ± 0.23	10.2 ± 1.1	–	–	–	–
1086	1.89 ± 0.31	9.3 ± 1.6	–	–	–	–
1112	1.99 ± 0.08	9.9 ± 0.4	–	–	–	–
1173	1.30 ± 0.10	6.5 ± 0.5	2.29 ± 0.16	11.72 ± 0.81	2.06 + 0.15	10.54 ± 0.73
1278	1.77 ± 0.21	9.5 ± 1.1	2.18 ± 0.16	11.61 ± 0.74	1.79 + 0.12	9.56 ± 0.70
1333	1.26 ± 0.08	6.9 ± 0.4	2.02 ± 0.13	11.01 ± 0.75	1.68 + 0.12	9.19 ± 0.67
1408	1.69 ± 0.24	9.5 ± 1.3	–	–	–	–

porosity estimated from Archimedes' method, pore volume and pore structure by mercury intrusion porosimetry, mechanical properties both cold modulus of rupture (CMOR) and cold crushing strength (CCS) of the concrete materials A, B and C were determined for samples sintered at 1400 °C. The results of the physical and mechanical characteristics of concretes are summarized in Table 4. These results generally indicate that the concrete materials are of acceptable quality for special construction applications.

Mercury porosimetry was found to be useful for characterizing the physical structure of porous ceramics [56]. The cumulative pore volume in dependence on the pore diameter and log differential volume −dV/d (log d) versus pore diameter were taken from mercury porosimetry data for each concrete material A-C after sintering at 1400 °C and were presented in Figs. 12 and 13, respectively. Pore frequency curves were derived from Fig. 12. As can be observed from these results, the concrete C possessed a slightly higher porosity than concretes A and B (Fig. 12) which was in accordance with the low magnification overview of SEM microstructure, see Fig. 8. Pore volume frequencies indicated a rather narrow range of pore sizes for all concrete samples (Fig. 13). It can be noted that for the present concretes A and C, most of the pore diameters are near 10 μm (Fig. 13). The concrete B exhibits a monomodal pore size distribution with a frequency peak below 10 μm.

3.3.3. Determination of the γ quanta attenuation properties of the studied concretes

Results of measurements of the linear attenuation coefficients are presented for all the three concretes before sintering and after this procedure in Fig. 14a–c and Fig. 14d–f, respectively. We have estimated both the statistical and systematic uncertainties. The latter ones come mainly from the radioactive source positioning (a few mm precision), the measurement of the samples thickness (~1 mm precision) and the used fitting method. As one can see the linear attenuation coefficients for all the concretes studied are systematically higher for materials before sintering which was expected since this process removes water while not changing significantly the density of the material. Apart from several energy ranges for which the attenuation coefficients are noticeably different there are no significant variation in the γ radiation attenuation between all the studied materials. The energy dependence of the attenuation coefficients were fitted using polynomial functions of degrees 1–3. This very simplified model was motivated taking into account the average atomic number of the studied materials and the energy range of used γ quanta for which Compton scattering is the dominating process of interaction. Although these fits are not describing the measured data very well, one can notice that the dependence for concrete B and C before sintering are very close and they change after applying this process.

For each γ quantum energy we have estimated mass attenuation coefficients using the densities of the tested materials presented in Table 4. They allowed for further calculation of total atomic cross sections, using Eq. (3), HLV parameters and effective atomic numbers of the tested concretes. The latter ones were estimated according to the logarithmic interpolation formula described in Ref. [34]:

$$Z_{eff} = \frac{Z_1(\log(\sigma_2) - \log(\sigma_a)) + Z_2(-\log(\sigma_1))}{\log\left(\frac{\sigma_2}{\sigma_1}\right)} \tag{4}$$

where σ_1 and σ_2 denote the maximum and minimum values of elemental cross sections for which $\sigma_1 < \sigma < \sigma_2$, respectively. Z_1 and Z_2 are the atomic numbers of elements corresponding to σ_1 and σ_2. The elemental cross sections used to estimate Z_{eff} were taken for every γ quantum line from the NIST database [57]. All the obtained results are gathered in Table 5 and Table 6 for samples before sintering and in Table 7 and Table 8 for samples after sintering. For samples before sintering concretes B and C exhibit in general better shielding properties than concrete A. This tendency remain unchanged even for samples examined after sintering and appear to be strongest in the low energy range up to 303 keV. Explanation of this effect may be found taking into account elemental composition of the studied materials given in Tables 2 and 3. Concretes B and C contain much more elements with high atomic number (Ba, Sr, Zr) than the material A. Probability of gamma quantum interaction depends strongly on the average atomic number of the absorbent, especially for lower energy region where the photoelectric effect is dominant. Thus, for materials B and C we observe increased shielding properties, especially at lower energies. Comparison of the obtained results with values stored in the NIST database [57] reveal a small improvement in the γ quanta attenuation for all the studied sample with respect to the ordinary concrete.

Since no data have been found in the literature on the gamma radiation shielding properties of concretes resistant to high temperatures, we propose new sintered materials in a form with the coarse corundum aggregate skeleton and ceramic matrix firmed via reactive sintering of fine grained components. Comparison of the gamma rays attenuation properties obtained for material C after sintering with other concretes studied in the literature is shown in Table 9 and Table 10. As one can see, the mass attenuation coefficients of the materials studied in this work are at the level of the values for other materials studied before. Moreover, we have determined the gamma rays attenuation properties in the energy region between 779 keV and 1112 keV which was not explored do far.

4. Conclusions

Results of the described research can be summarized with the following conclusions:

1. New hydraulic cements belonging to $CaO–Al_2O_3$, $SrO–Al_2O_3$, $SrO–CaO–Al_2O_3–ZrO_2$ and $BaO–CaO–Al_2O_3–ZrO_2$ systems designed for shielding concretes were developed as an alternative binders to ordinary Portland cement (OPC) heavy concretes.
2. The high purity corundum was used as an aggregate to assess the gamma radiation shielding performance of these cements.
3. The doping alkaline earth elements Sr and Ba were chemically bonded within both hydrated cement matrix and the ceramic matrix of concrete formed through sintering at 1400 °C. It was found that the incorporation of Sr or Ba and Zr elements with cements improved the attenuation properties of corundum-based concretes, in comparison to the concretes with the predominance of Ca.
4. The concrete matrix partly consolidated through sintering varied depending on the raw materials used. Strontium was able to substitute for calcium in calcium hexaaluminate to form a $(C,Sr)A_6$ solid solution. The main feature of barium is that it formed its barium aluminum silicate phase BAS_2. Since calcium zirconium aluminate was used as a binder additive, ZrO_2 was formed as a secondary phase in the concrete matrix (concretes B and C). Since microsilica was used to improve the flowing characteristics, gehlenite C_2AS was also formed in the sintered concrete matrix.

5. A better performance in gamma-ray shielding was achieved for unfired concretes dried at 110 °C compared to concretes sintered at 1400 °C.
6. Gamma-ray-attenuation measurements using 22Na, 137Cs, 60Co, 133Ba and 152Eu sources gave results which showed that the gamma-ray attenuation of the studied concretes was improved as compared with ordinary concrete presented in the National Institute of Standards and Technology (NIST) database [57]. Our work fills the gap in the literature providing the gamma rays attenuation properties of new cement-containing heat-resistant corundum concretes in the energy region between 779 keV and 1112 keV. These concretes have so far not been proposed as shielding materials.

CRediT authorship contribution statement

Dominika Madej: Conceptualization, Data curation, Formal analysis, Funding acquisition, Investigation, Methodology, Project administration, Resources, Software, Supervision, Validation, Visualization, Writing - original draft, Writing - review & editing. **Michał Silarski:** Formal analysis, Funding acquisition, Investigation, Methodology, Resources, Software, Validation, Visualization, Writing - review & editing. **Szymon Parzych:** Investigation.

Declaration of competing interest

The authors declare that they have no known competing financial interests or personal relationships that could have appeared to influence the work reported in this paper.

Acknowledgements

References

[1] P. Prochon, T. Piotrowski, The effect of cement and aggregate type and w/c ratio on the bound water content and neutron shielding efficiency of concretes, Construct. Build. Mater. 264 (2020) 120210, https://doi.org/10.1016/j.conbuildmat.2020.120210.

[2] O. Lotfi-Omran, A. Sadrmomtazi, I.M. Nikbin, The influences of maximum aggregate size and cement content on the mechanical and radiation shielding characteristics of heavyweight concrete, Prog. Nucl. Energy 121 (2020) 103222, https://doi.org/10.1016/j.pnucene.2019.103222.

[3] O. Lotfi-Omran, A. Sadrmomtazi, I.M. Nikbin, A comprehensive study on the effect of water to cement ratio on the mechanical and radiation shielding properties of heavyweight concrete, Construct. Build. Mater. 229 (2019) 116905, https://doi.org/10.1016/j.conbuildmat.2019.116905.

[4] A.T. Şensoy, H.S. Gökçe, Simulation and optimization of gamma-ray linear attenuation coefficients of barite concrete shields, Construct. Build. Mater. 253 (2020) 119218, https://doi.org/10.1016/j.conbuildmat.2020.119218.

[5] M.U. Khan, S. Ahmad, A.A. Naqvi, H.J. Al-Gahtani, Shielding performance of heavy-weight ultra-high-performance concrete against nuclear radiation, Prog. Nucl. Energy 130 (2020) 103550, https://doi.org/10.1016/j.pnucene.2020.103550.

[6] M.H. Kharita, S. Yousef, M. AlNassar, The effect of the initial water to cement ratio on shielding properties of ordinary concrete, Prog. Nucl. Energy 52 (5) (2010) 491–493, https://doi.org/10.1016/j.pnucene.2009.11.005.

[7] İ. Demir, M. Gümüş, H.S. Gökçe, Gamma ray and neutron shielding characteristics of polypropylene fiber-reinforced heavyweight concrete exposed to high temperatures, Construct. Build. Mater. 257 (2020) 119596, https://doi.org/10.1016/j.conbuildmat.2020.119596.

[8] Raizal S.M. Rashid, S. Mohammed Salem, N.M. Azreen, Y.L. Voo, M. Haniza, A. A. Shukri, Mohd-Syukri Yahya, Effect of elevated temperature to radiation shielding of ultra-high performance concrete with silica sand or magnetite, Construct. Build. Mater. 262 (2020) 120567, https://doi.org/10.1016/j.conbuildmat.2020.120567.

[9] B. Aygün, Neutron and gamma radiation shielding properties of high-temperature-resistant heavy concretes including chromite and wolframite, J. Radiat. Res. Appl. Sc. 12 (1) (2019) 352–359, https://doi.org/10.1080/16878507.2019.1672312.

[10] K. Singh, S. Singh, A.S. Dhaliwal, G. Singh, Gamma radiation shielding analysis of lead-flyash concretes, Appl. Radiat. Isot. 95 (2015) 174–179, https://doi.org/10.1016/j.apradiso.2014.10.022.

[11] J.F. Lamond, J.H. Pielert, Significance of Tests and Troperties of Concrete and Concrete-Making Materials, ASTM International, 2006.

[12] W. Gu, L. Zhu, X. Shang, D. Ding, L. Liu, L. Chen, G. Ye, Effect of particle size of calcium aluminate cement on volumetric stability and thermal shock resistance of CAC-bonded castables, J. Alloys Compd. 772 (2019) 637–641, https://doi.org/10.1016/j.jallcom.2018.09.128.

[13] M. Nematzadeh, J. Dashti, B. Ganjavi, Optimizing compressive behavior of concrete containing fine recycled refractory brick aggregate together with calcium aluminate cement and polyvinyl alcohol fibers exposed to acidic environment, Construct. Build. Mater. 164 (2018) 837–849, https://doi.org/10.1016/j.conbuildmat.2017.12.230.

[14] W. Khaliq, H. Anis Khan, High temperature material properties of calcium aluminate cement concrete, Construct. Build. Mater. 94 (2015) 475–487, https://doi.org/10.1016/j.conbuildmat.2015.07.023.

[15] P. Ptáček, in: P. Ptacek (Ed.), Applications of Strontium Aluminate Cements, Strontium Aluminate - Cement Fundamentals, Manufacturing, Hydration, Setting Behaviour and Applications, IntechOpen, 2014, pp. 141–185.

[16] P. Ptáček, F. Šoukal, T. Opravil, E. Bartoníčková, M. Zmrzlý, R. Novotný, Synthesis, hydration and thermal stability of hydrates in strontium-aluminate cement, Ceram. Int. 40 (2014) 9971–9979, https://doi.org/10.1016/j.ceramint.2014.02.095.

[17] H. Pöllmann, S. Stöber, P. Mohr, R. Kaden, in: C.H. Fentiman, R. Mangabhai, K. L. Scrivener (Eds.), Synthesis and Crystal Chemistry of Strontium Aluminates, Calcium Aluminates: Proceedings of the International Conference, IHS BRE Press, Garston, Watford, UK, 2014, pp. 89–98.

[18] H. Pöllmann, R. Kaden, Mono- (strontium-, calcium-) aluminate based cements, in: ChH. Fentiman, R. Mangabhai, K.L. Scrivener (Eds.), Calcium Aluminates: Proceedings of the International Conference, IHS BRE Press, Garston, Watford, UK, 2014, pp. 89–98.

[19] A.K. Prodjosantoso, B.J. Kennedy, Synthesis and evolution of the crystalline phases in Ca$_{1-x}$Sr$_x$Al$_2$O$_4$, J. Solid State Chem. 168 (2002) 229–236, https://doi.org/10.1006/jssc.2002.9715.

[20] S.H. Ju, S.G. Kim, J.C. Choi, H.L. Park, S.I. Mho, T.W. Kim, Determination of the solid solubility of SrAl$_2$O$_4$ in CaAl$_2$O$_4$ through crystal field-dependent Eu^{2+} signatures, Mater. Res. Bull. 34 (1999) 1905–1909, https://doi.org/10.1016/S0025-5408(99)00201-9.

[21] A.K. Prodjosantoso, B.J. Kennedy, Solubility of SrAl$_2$O$_4$ in CaAl$_2$O$_4$ – a high resolution powder diffraction study, Mater. Res. Bull. 38 (2003) 79–87, https://doi.org/10.1016/S0025-5408(02)01009-7.

[22] H. Pöllmann, R. Kaden, X-ray investigations of solid solutions and phase transitions of monocalciumaluminate and monobariumaluminate-use in cement, phosphorescence and radiation protection applications, Adv. X Ray Anal. 59 (2016) 176–191.

[23] M.R. Rezaie, H.R. Rezaie, R. Naghizadeh, The effect of SiO$_2$ additions on barium aluminate cement formation and properties, Ceram. Int. 35 (2009) 2235–2240, https://doi.org/10.1016/j.ceramint.2008.12.009.

[24] P.P. Budnikov, V.G. Savel'yev, Refractory concretes with a barium aluminate binder, Refractories-USSR+ 3 (1962) 314–317, https://doi.org/10.1007/BF01342802.

[25] T.J. Davies, W.A. Al-Douri, M. Biedermann, Q.G. Chen, H.G. Emblem, Refractory oxides containing barium, J. Mater. Sci. Lett. 15 (1996) 482–484, https://doi.org/10.1007/BF00275408.

[26] N.M. Khalil, Refractory concrete based on barium aluminate-barium zirconate cements for steel-making industries, Ceram. Int. 31 (2005) 937–943, https://doi.org/10.1016/j.ceramint.2004.09.020.

[27] D. Madej, R. Boris, Synthesis, characterization and hydration analysis of Ba^{2+}-, Cu^{2+}- or Bi^{3+}-doped CaO-Al$_2$O$_3$-ZrO$_2$-based cements, J. Therm. Anal. Calorim. 138 (2019) 4331–4340, https://doi.org/10.1007/s10973-019-08142-7.

[28] D. Madej, A. Kruk, Monitoring hydration of Sr-doped calcium zirconium aluminate (Ca,Sr)7ZrAl6O18 cement via electrochemical impedance spectroscopy (EIS) and supported techniques, Construct. Build. Mater. 206 (2019) 307–320, https://doi.org/10.1016/j.conbuildmat.2019.02.073.

[29] D. Madej, Synthesis and hydraulic activity of novel Sr2+-doped Ca7ZrAl6O18 cement at 50°C, Thermochim. Acta 661 (2018) 98–105, https://doi.org/10.1016/j.tca.2017.12.001.

[30] D. Madej, Hydration, carbonation and thermal stability of hydrates in Ca$_{7-x}$Sr$_x$ZrAl$_6$O$_{18}$ cement, J. Therm. Anal. Calorim. 131 (2018) 2411–2420, https://doi.org/10.1007/s10973-017-6726-1.

[31] D. Madej, A new implementation of electrochemical impedance spectroscopy (EIS) and other methods to monitor the progress of hydration of strontium monoaluminate (SrAl$_2$O$_4$) cement, J. Therm. Anal. Calorim. 139 (1) (2020) 17–28, https://doi.org/10.1007/s10973-019-08423-1.

[32] https://www.ortec-online.com/-/media/ametekortec/brochures/gamma-x-a4.pdf.

[33] Z. Guzik, S. Borsuk, K. Traczyk, M. Plominski, TUKAN-an 8K pulse height analyzer and multi-channel scaler with a PCI or a USB interface, IEEE Trans. Nucl. Sci. 53 (1) (2006) 231–235.

[34] M. Kurudirek, M. Aygun, S.Z. Erzeneoglu, Chemical composition, effective atomic number and electron density study of trommel sieve waste (TSW), Portland cement, lime, pointing and their admixtures with TSW in different proportions, Appl. Radiat. Isot. 68 (2010) 1006–1011.

[35] A.H. Moinuddin Ahmed, L.S. Dent Glasser, Barium aluminate hydrates. I. A barium analogue of hydrogarnet, Acta Crystallogr. B25 (1969) 2169–2170, https://doi.org/10.1107/S0567740869005358.

[36] A.H.M. Ahmed, L.S. Dent Glasser, Barium aluminate hydrates I. General survey and preparative methods, J. Appl. Chem. Biotechnol. 21 (1971) 103–106, https://doi.org/10.1002/jctb.5020210404.

[37] A.H.M. Ahmed, L.S. Dent Glasser, Barium aluminate hydrates II. BaO•Al$_2$O$_3$•H$_2$O or 1.1BaO•Al$_2$O$_3$•H$_2$O, J. Appl. Chem. Biotechnol. 21 (1971) 107–108, https://doi.org/10.1002/jctb.5020210405.

[38] A.H.M. Ahmed, L.S. Dent Glasser, Barium aluminate hydrates. II. The crystal structure of Ba2[Al2(OH)10], Acta Crystallogr. B26 (1970) 867–871, https://doi.org/10.1107/S0567740870003254.

[39] A.H.M. Ahmed, L.S. Dent Glasser, Barium aluminate hydrates. III. The crystal structure of α-Ba[AlO(OH)2]2, Acta Crystallogr. B. 26 (1970) 1686–1690.

[40] A.H.M. Ahmed, L.S. Dent Glasser, Barium aluminate hydrates III. BaO•Al$_2$O$_3$•2H$_2$O and BaO•Al$_2$O$_3$•0.5H$_2$O, J. Appl. Chem. Biotechnol. 21 (1971) 109–112, https://doi.org/10.1002/jctb.5020210406.

[41] A.H. Moinuddin Ahmed, L.S. Dent Glasser, Barium aluminate hydrates IV. α-BaO•Al$_2$O$_3$•4H$_2$O, J. Appl. Chem. Biotechnol. 23 (1973) 457–463, https://doi.org/10.1002/jctb.5020230608.

[42] L.S. Dent Glasser, R. Giovanol, Barium aluminate hydrates. IV. The crystal structure of α-Ba2[AI4(OH)16], Acta Crystallogr. B28 (1972) 519–524, https://doi.org/10.1107/S0567740872002675.

[43] A.H. Moinuddin Ahmed, L.S. Dent Glasser, Barium aluminate hydrates: Part V. 2BaO·Al2O3·2H2O and 2BaO·Al2O3, J. Appl. Chem. Biotechnol. 42 (1988) 31–38, https://doi.org/10.1002/jctb.280420105.

[44] L.S. Dent Glasser, R. Giovanoli, Barium aluminate hydrates. V. The crystal structure of γ-Ba[AIO(OH)2]2, Acta Crystallogr. B28 (1972) 760–763, https://doi.org/10.1107/S0567740870004739.

[45] A.H. Moinuddin Ahmed, L.S. Dent Glasser, Barium aluminate hydrates-VI. 2BaO•Al$_2$O$_3$•5H$_2$O and 2BaO•Al$_2$O$_3$•H$_2$O, J. Appl. Chem. Biotechnol. 45 (1989) 303–309, https://doi.org/10.1002/jctb.280450407.

[46] A.H.M. Ahmed, L.S.D. Glasser, M.G. King, Barium aluminate hydrates. VI. The crystal structure of BaO•Al$_2$O$_3$•H$_2$O, Acta Crystallogr. 29 (1973) 1166–1167.

[47] M.C. Cruickshank, L.S. Dent Glasser, R.A. Howie, The structure of barium aluminate hydrate, 2BaO•5AI$_2$O$_3$•H$_2$O Acta Cryst. C41 (1985) 159–161, https://doi.org/10.1107/S0108270185003146.

[48] E.T. Carlson, L.S. Wells, Barium aluminate hydrates, Research Paper RP1908 41 (1978) 103–109.

[49] D. Madej, Synthesis, formation mechanism and hydraulic activity of novel composite cements belonging to the system CaO-Al$_2$O$_3$-ZrO$_2$, J. Therm. Anal. Calorim. 130 (3) (2017) 1913–1924, https://doi.org/10.1007/s10973-017-6498-7.

[50] J. Szczerba, D. Madej, K. Dul, P. Bobowska, Ca$_7$ZrAl$_6$O$_{18}$ acting as a hydraulic and ceramic bonding in the MgO-CaZrO$_3$ dense refractory composite, Ceram. Int. 40 (5) (2014) 7315–7320, https://doi.org/10.1016/j.ceramint.2013.12.073.

[51] P. Tarte, Infra-red spectra of inorganic aluminates and characteristic vibrational frequencies of AlO$_4$ tetrahedra and AlO$_6$ octahedra, Spectrochim. Acta A-M 23 (7) (1967) 2127–2143, https://doi.org/10.1016/0584-8539(67)80100-4.

[52] G.D. Chukin, Yu L. Seleznev, Mechanism of the thermal decomposition of boehmite and a structural model of aluminum oxide, Kinet. Katal. 30 (1) (1989) 69–77.

[53] J. Chandradass, D.S. Bae, K.H. Kim, Synthesis of calcium hexaaluminate (CaAl$_{12}$O$_{19}$) via reverse micelle process, J. Non-Cryst. Solids 355 (2009) 2429–2432, https://doi.org/10.1016/j.jnoncrysol.2009.08.032.

[54] A.M. Hofmeister, B. Wopenka, A.J. Locock, Spectroscopy and structure of hibonite, grossite, and CaAl$_2$O$_4$: implications for astronomical environments, Geochem. Cosmochim. Acta 68 (21) (2004) 4485–4503, https://doi.org/10.1016/j.gca.2004.03.011.

[55] C.M. Phillippi, K.S. Mazdiyasni, Infrared and Raman spectra of zirconia polymorphs, J. Am. Ceram. Soc. 54 (5) (1971) 254–258, https://doi.org/10.1111/j.1151-2916.1971.tb12283.x.

[56] O.J. Whittemore, Mercury porosimetry of ceramics, Powder Technol. 29 (1) (1981) 167–175, https://doi.org/10.1016/0032-5910(81)85014-0.

[57] J. H. Hubbell+ and S. M. Seltzer, Tables of X-ray mass attenuation coefficients and mass energy-absorption coefficients from 1 keV to 20 MeV for elements Z = 1 to 92 and 48 additional substances of dosimetric Interest,Radiation Physics division, PML, NIST (DOI: https://dx.doi.org/10.18434/T4D01F).

[58] N. Damla, H. Baltas, A. Celik, E. Kırıs, U. Cevik, Calculation of radiation attenuation coefficients, Effective atomic numbers and electron densities for some building materials, Radiat. Protect. Dosim. 150 (4) (2012) 541–549, https://doi.org/10.1093/rpd/ncr432.